ELECTRICAL CHARACTERIZATION OF 1 X 2 COHERENT VCSEL ARRAYS

By

Joseph Hwang

Senior Thesis in Electrical Engineering

University of Illinois at Urbana-Champaign

Advisor: Professor Kent D. Choquette

May 2019

Abstract

Two adjacent semiconductor vertical cavity surface-emitting lasers (VCSELs) can be tuned to coherent operation where optically-coupled VCSELs exhibit array “super-modes”, unique from individual laser cavity optical modes. Coherent VCSEL arrays have several important device properties for potential applications including increasing intensity modulation rate for high speed optical communications and all-optical beam-steering. Currently, however, coherently coupled operation is only recognized from far-field optical intensity distribution measurements.

This thesis reports the investigation of both optical and electrical characteristics of 2 x 1 VCSEL arrays to identify an electrical “signature” or series resistance features in coupled lasers as a means for detecting and biasing to coherent operation. Measurement methods using two varying inputs for characterizing the VCSEL arrays are demonstrated and a voltage derivative analysis is presented.

Subject Keywords: semiconductor lasers; photonics; VCSEL; laser arrays; electrical derivative analysis; coherently coupled arrays

Acknowledgements

I would first like to acknowledge Professor Kent D. Choquette, principal investigator of the Photonic Device Research Group and my advisor throughout this work. I also want to offer my sincerest gratitude to graduate researcher, Harshil Dave. They have provided invaluable mentorship and advice throughout my undergraduate research experiences are responsibly for helping form my unique perspective as an experimental researcher. I will always carry with me the wisdom they have offered, both in life and work. I want to thank Katie Lakomy for offering advice, buying me Panera on multiple occasions, and revising my slides and figures and to recognize the rest of the Photonic Device Research Group: Brad Thompson, Pawel Strzebonski, and Sanat Pandey, as well as alumnus Zihe Gao. They have all added to this work and my experience in the group.

Contents

1. Introduction

Vertical cavity surface-emitting lasers (VCSELs) were invented in 1979, 17 years after the original semiconductor laser, by Professor Kenichi Iga at the Tokyo Institute of Technology who envisioned a semiconductor microcavity laser that would emit perpendicular to the wafer surface, rather than parallel to it [1].

VCSELs have become a little-known powerhouse component of the internet infrastructure. The internet is composed of a massive interconnected series of networks that transfer information globally. This information is stored in data centers at the local area or storage area network level, where information is moved around internally through a series of optical fibers and interconnects many of which are driven by VCSELs [2]. By 2013, over a billion VCSELs were deployed in just 20 years for these short-reach optical communication and optical tracking systems, mostly lasing at 850 nm wavelength [2]. VCSELs have special advantages over the traditional edge-emitting lasers, including highly circularly symmetric beam emission profiles, ultralow power operation, easy integration into one- or two-dimensional arrays, and potential for low-cost, high-volume manufacturing [3]. This latter characteristic has pretty much been realized as major corporations such as Finisar, Phillips, and Broadcom (formerly Avago Technologies) manufacture and deploy over 650 million VCSELs annually.

1.1 Motivation

Commercial development of VCSELs today focuses primarily on arrays, multiple VCSEL elements operating together. With continued efforts in VCSEL arrays, the industry has experienced a second explosion as novel consumer electronic technologies are becoming realized with VCSEL arrays as the

light source in applications such as in 3D imaging, LIDAR sensing, and proximity sensing. In 2017, Apple released the iPhone X which featured three integrated VCSEL array chips for 3D facial identification (Face ID) and proximity sensing. This market is expected to expand to over 3 billion units deployed in 2024 [4]. Figure 1.1 is an image of the dot projector that forms the infrared pattern used by the iPhone for facial recognition [5].

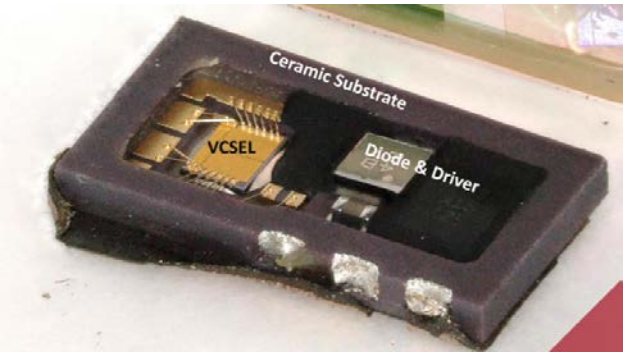

Figure 1.1 NIR dot projector in the iPhone X for Face ID. Image courtesy of Systems Plus Consulting [5]

Aside from these emerging applications, VCSELs continue to push the boundaries of optical communications. Present day data centers employ VCSELs that can achieve modulation rates of up to 28 Gbps. Higher digital modulation rates require ever greater bandwidth. Recent work in the Photonics Device Research Group has demonstrated that single 2 x 1 VCSEL arrays, operating in coherent coupling modes, feature modulation bandwidth enhancement up to 37 GHz [6, 7].

Until this work, coherently coupled operation has only been recognizable in the near-field and far-field spatial distributions as well as the output intensity, as will be discussed in Chapter 2. These all require measurements of the optical output in some form or other. An electrical detection scheme is desirable for practical systems when it is necessary to maintain coherent coupling between the

elements. Therefore, the goal of this thesis is to determine whether coupling can be recognized in the electrical measurements of 1x2 VCSEL arrays and to characterize its behavior. In the remainder of this chapter, semiconductor lasers and VCSELs will be reviewed. This chapter is followed by a chapter review of relevant literature and previous work, a chapter discussing the experimental methods involved in array characterization, and finally an analysis and summary of the results.

1.2 Technical Background

Lasers are coherent light sources composed of three basic components: 1) a gain medium, 2) an optical cavity, and 3) a pump for achieving the stimulated emission of electromagnetic radiation (light). Semiconductors offer a powerful avenue for engineering all three of these by designing indices of refraction profiles and tuning electrical characteristics through modern fabrication techniques. Semiconductor structures achieve lasing through spectral and spatial overlap of the cavity resonance and gain. Laser emission is composed of spontaneous and stimulated emission. Spontaneous emission occurs from the random recombination of electrons and holes. The spontaneously emitted photons that are emitted into the lasing mode possess various phases and are thus incoherent. In stimulated emission, a photon stimulates the carrier recombination that generates a photon of the same phase as the original photon. Lasing operation requires injecting and confining enough electrons to achieve population inversion. To have stimulated emission dominate, an optical cavity, typically two parallel mirrors, are needed to trap photons within the medium so that it can generate more coherent photons. In compound semiconductors, epitaxial compositional heterostructures provide the means for varying the index of refraction in order to engineer this reflection. When current injection provides enough gain to dominate loss and stimulated emission dominates in the cavity, this is known as the lasing threshold.

Figure 1.2 shows the cross section of the two neighboring VCSELs [7]. In most VCSELs that nominally emit at 850nm the gain medium is a gallium arsenide quantum well bounded by the cavity mirrors. In a VCSEL the cavity mirrors are parallel to the wafer surface so that emission occurs perpendicular to the surface as shown in Fig. 1.2 [3]. The desired reflectivity of both cavity mirrors should approach but not reach unity (100%). The index contrast provided by semiconductor/air interface along cannot provide this. Instead the high reflectivity mirrors are formed by a distributed Bragg reflector (DBR). This is produced by epitaxially grown quarter-wavelength thick layers of varying compositions of $Al_xGa_{1-x}As$. The total reflection is added constructively across multiple high-low index interfaces within the DBR for high total reflectivity. As a helpful consequence, a pair of DBRs separated appropriately can create a single longitudinal mode [3].

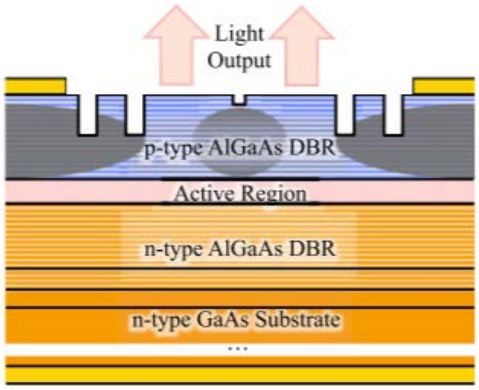

Figure 1.2 Cross-sectional schematic of a 2x1 VCSEL array. The individual layers of the DBR can be seen. [7]

2. Review of Literature and Future Work

In this chapter, previous research discussed in the literature related to this project is summarized. Two topics are covered: the theory underlying the operation of photonic crystal VCSEL arrays in coherent operation and the experimental technique of electrical derivative analysis which has been previously used to correlate electrical characteristics with optical phenomena in semiconductor laser diodes. These topics of research both serve as the foundation for the experimental work presented in this thesis. This project is part of, and built on, a larger body of work conducted at the Photonic Device Research Group at the University of Illinois. Shown in Fig. 2.1 is an image of the 2x1 VCSEL arrays characterized in this project [7].

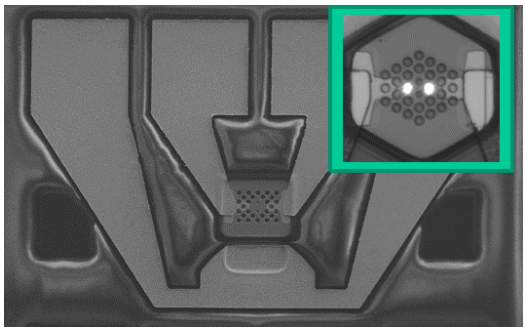

Figure 2.1 Image of 2x1 VCSEL array characterized in this project; (inset) close-up of the VCSEL elements surface where both cavities as shown lasing as the two white dots [7].

2.1 Coherently-Coupled VCSEL Arrays

In conventional single element microcavity lasers, each laser emits light in one or more optical modes. For VCSELs, which are designed to support a single longitudinal mode in the direction of propagation, the additional modes are transverse modes which are the fields transverse to the direction of propagation. Though a VCSEL may be designed to nominally emit at 850 nm wavelength, the supported transverse modes will have slightly differing emission wavelengths. When a laser enters stimulated emission, each photon is emitted into one of these supported modes, and the photons that constitute the emission of any given optical mode are identical and thus we can say they are coherent with each other. Coherence, considered classically, refers to a phase relationship between two different points of an electric-field or intensity distribution, temporally or spatially. From a quantum optics perspective, coherence can be defined spatially or spectrally. In a simple sense, the manifestation of spatial coherence between two light sources is a structured interference pattern, including fringes, in the far-field [8]. The model paradigm for a pair of emitters is the interference pattern from Young's double slit experiment. Observing such a structured far-field from a supermode is the standard by which we consider the two elements of the array to be operating in a "coherently coupled" manner.

Figure 2.2 illustrates the transverse electric field profile under evanescent coupling between two cavities. The burgundy curves show two fundamental modes confined to each cavity, acting independent of each other. The green curve shows the field profile when evanescent coupling forms a supermode that exists in both cavities. Electromagnetic fields in a semiconductor laser cavity are not perfectly confined. In a VCSEL array, evanescent "tails" extend into the material between two cavities. If the cavities are sufficiently close together, photons can tunnel from one cavity to the next, and a "super mode" can be formed. Figure 2.2 shows an example of an out-of-phase supermode in green. For the photonic crystal VCSEL arrays studied here, the coupling occurs due to anti-guiding effects from the

higher refractive index region between the cavities, and the supermode formation is similar but enhanced as compared to evanesent optical coupling [9].

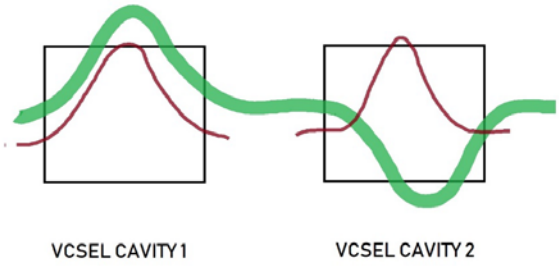

Figure 2.2 Schematic drawing of a coupled out-of-phase "supermode" in a cavity (green) in contrast to typical individual laser modes (burgundy).

Figure 2.3 illustrates two VCSEL elements and the three kinds of far-field intensity profiles they can emit [10, 11]. If the two elements are above lasing threshold, but each laser is independent of the other, then each element emits into the lowest order cavity mode, the Gaussian mode. The dashed black line shows the overlapping Gaussian emission from each laser when the lasers are not coupled. In this mode of operation, because the emissions of the two lasers are not coherently coupled, the spatial profile that arises in the far-field is without fringes and appears as a simple Gaussian-like distribution, like the dashed black line in Fig. 2.3. Note that the divergence of the individual Gaussian modes as measured by the far-field can be > 20°. However, if the two elements are optically coupled, then the supermode overlaps both elements: the orange and blue curves in Fig. 2.3 show the two possible far-field distributions of the coupled supermodes. In coupled operation, photons emitted from one cavity will have a strong spatial phase relationship with photons emitted from the other. This spatial coherence extends to the far-field, exhibiting a structured far-field distribution like those drawn in orange and blue in Figure 2.3. Because these modes are unique from the cavity modes created by independent lasers,

and because they are not spatially restricted but extend over all of the array elements, they are referred to as “supermodes.” The orange curve is an in-phase coupled mode which arises when the electric fields in each cavity are equal. Like the Gaussian mode, it features an on-axis peak, with the addition of subsidiary side lobes [10]. Notice the central lobe of the in-phase emission has a much smaller divergence angle which arises from the optical coupling. The blue curve is an out-of-phase coupled mode defined by an on-axis null with off-axis emission peak. Shown in Fig. 2.3 are examples of these experimentally measured far-field modes.

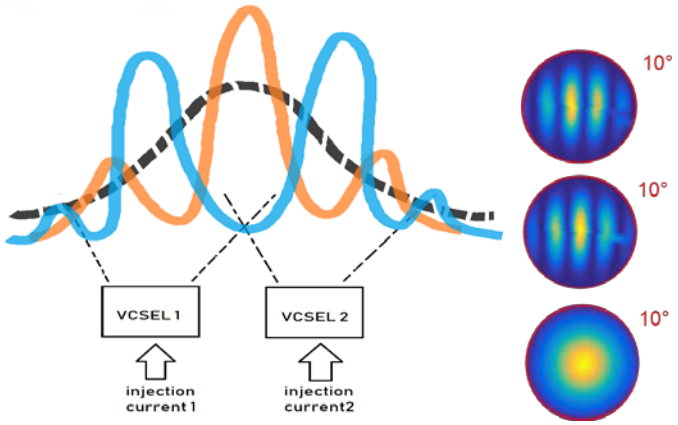

Figure 2.3 (Left) Sketch of far-field mode profiles from a two-element VCSEL array: Gaussian (black dashed), In-Phase coupled (orange), and out-of-phase coupled (blue). The three images on the right are experimentally measured far-field modes: out-of-phase super-mode (top) in-phase super-mode (middle) and incoherent (bottom).

Previous work in the Photonic Device Research Group has identified a characteristic “peak” in the light vs. current (L-I) of 1x2 VCSEL arrays that has been correlated to the onset of coherent coupled operation of the array [12]. Figure 2.4 is an example of the measured output intensity from a 1x2 array where one injection current is fixed (I_2) and the other (I_1) is varied. This region of increased power has been confirmed to align with coupled mode operation and the increase in power itself has been used to

calculate the imaginary part of the coupling coefficient [12]. It can, therefore, be considered a measure of the degree of coupling.

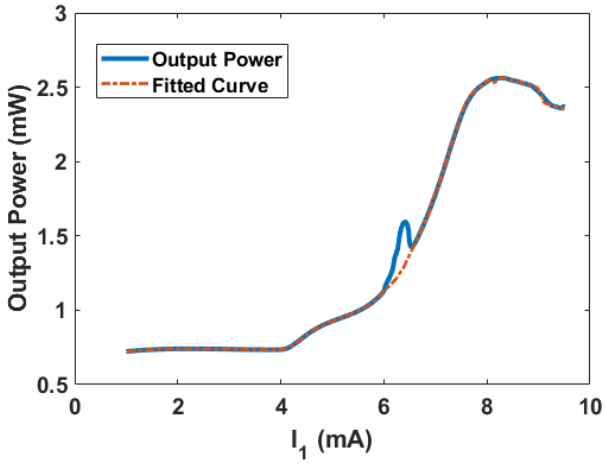

Figure 2.4 Light output versus I_1 for fixed I_2 illustrating the intensity "peak" at approximately 6.2 mA that arises from optical coupling between the two elements.

2.2 Electrical Derivative Analysis

Electrical derivative analysis (EDA) is a technique that has been used to identify the threshold current of semiconductor laser devices [13-17]. It is also applicable for correlating electrical and optical characteristics of VCSELs as demonstrated by the late distinguished former ECE Illinois faculty member Professor Shun Lien Chuang [17]. Figure 2.5 is a reproduction from Prof. Chuang's research that shows the application of this technique to a single VCSEL [17]. The *IdV/dI* curve (solid), as well as polarization-resolved light outputs with varying injection current I, of a single selectively oxidized VCSEL fabricated at the University of Illinois is depicted in Fig. 2.5. This plot shows kinks in the *IdV/dI* curves that align with the threshold of lasing of the fundamental mode, the threshold for higher modes, and the end of

stimulated emission after the intensity reaches a maximum and rolls over. Figure 2.6 is an example of the EDA applied to an oxide-confined VCSEL in this present work. In Fig. 2.6 both the light output (red) and the I^2dV^2/dI^2 (blue) versus current curves are shown. The analysis described in this thesis is based on the precedent set by the electrical derivative analysis.

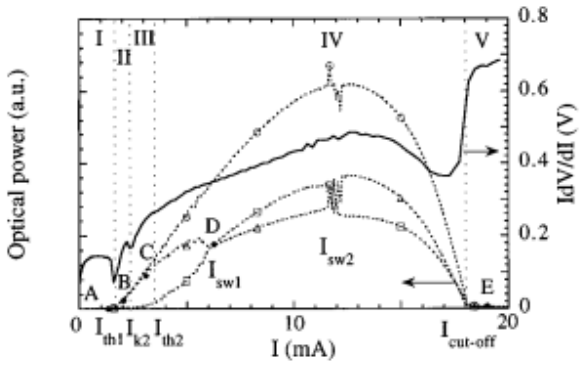

Figure 2.5 IdV/dI vs I for single oxide-confined VCSEL (solid) with polarization-resolved light outputs (dotted lines with triangles: parallel polarization, squares: perpendicular polarization, circles: total output) [17]

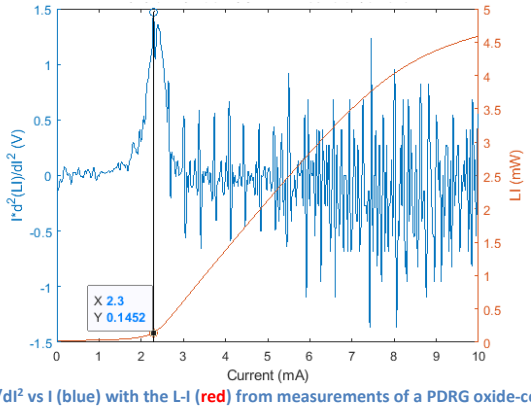

Figure 2.6 I^2dV^2/dI^2 vs I (blue) with the L-I (red) from measurements of a PDRG oxide-confined VCSEL

3. Experimental Methods

In this chapter the measurement procedures are described for collecting data. The sample of VCSEL devices, from which measurements were acquired, will also be described. A unique aspect of these measurements isthe use of two varying input currents. As will be shown in the next chapter, the resulting 2-dimensional analysis produces an electrical signature that identifies coherent operation.

3.1 Wafer Layout and Design

The 1x2 VCSEL array mask set that created the VCSEL array shown in Fig. 2.1 was designed and fabricated in 2016 by previous graduate students in the Photonic Device Research Group [7]. The cross-section schematic of an array is shown in Fig. 1.2 and a device under test is shown in Fig. 3.1. The individual elements of each array are designed to nominally emit at 850 nm wavelength. The semiconductor lasers are fabricated on a gallium arsenide (GaAs) substrate and consist of an active region surrounded by an upper p-type distributed Bragg reflector (DBR) mirror and lower n-type DBR mirror for longitudinal mode confinement. The top DBR mirror is etched with a hexagonal pattern of holes creating a photonic crystal (PhC) on the top mirror that induces transverse optical confinement in the inset of Fig. 2.1. The electrical confinement is independently defined by proton ion-implantation with independent addressability [7].

With the etched photonic crystal, a pair of elements in an array can be defined as shown in Fig. 1.2. The two elements within a single array are isolated electrically via a column of implants between them as sketched in Fig. 1.2. The PhC patterns also suppress higher-order modes for more dominant fundamental-mode lasing in each element. Two gold contacts are placed to bias each element, thus each device can be tested on wafer (see Fig. 3.1) using two signals surrounded by ground, as apparent in

Fig. 3.2(b). Light is output through the uppermost p-DBR mirror, emitting from the top surface of the wafer. A complete description of these devices can be found in [7].

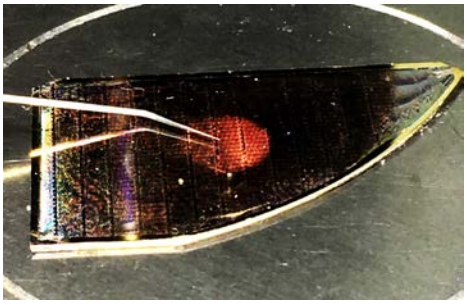

Figure 3.1 A 2 x 1 array device under wafer-level testing [7].

Figure 3.1 shows an image of the wafer from which devices were measured. Each rectangular corresponds to a cell of VCSEL array devices, consisting of one hundred 2 x 1 array devices of varying PhC patterns and transverse aperture sizes. An example of an individual array is shown below in Fig. 3.2. The two regions without PhC holes in the middle of the etch pattern, in Fig. 3.2(a), correspond to the optical emission regions of the two laser elements.

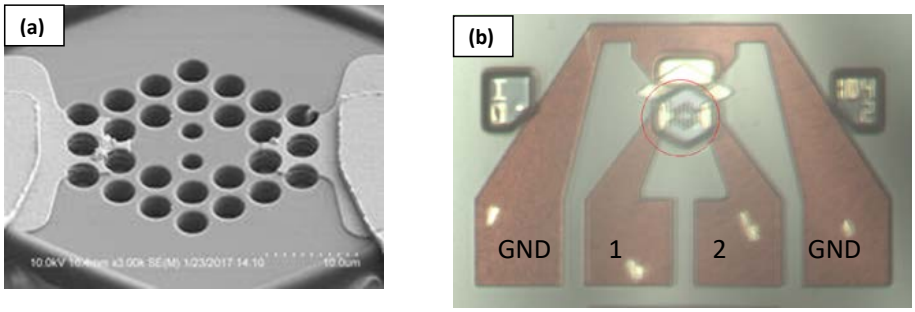

Figure 3.2 (a) SEM top view of 2x1 array defined by photonic crystal. (b) VCSEL array with ground-signal-signal-ground electrical contracts. The red circle in (b) corresponds to the view in (a).

3.2 Electrical and Optical Measurement

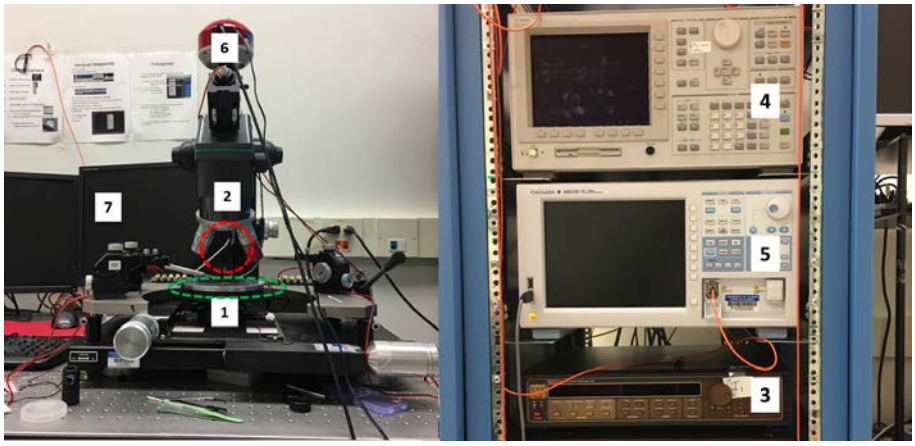

Figure 3.3 West Alessi Probe Station used for DC electrical and optical measurements. Setup includes: (1) vacuum sample stage in dashed green circle with probes, (2) photodetector, attached to the objective turret in dashed red circle with white optical fiber, (3) Keithly source measurement unit (SMU) , (4) Agilent semiconductor parametric analyzer (SPA), (5) Yokogawa optical spectrum analyzer (OSA), (6) CMOS camera, and (7) LabVIEW-equipped computer workstation.

Figure 3.2(a) shows an SEM image of the PhC-defined VCSEL top surface with the optical output of the elements circled in green, and Fig. 3.2(b) shows an overall view of the VCSEL array with its elements, contacts, and device addressing. The probe station used for DC optical and electrical measurements is shown in Fig. 3.3. The sample is placed on the vacuum chuck of the Alessi microscope probe station. Three probes shown in Fig. 3.3 are used to connect the ground (GND), the left laser element (1), and the right laser element (2) contacts on the wafer to a common ground, Keithley source measurement unit, and the Agilent semiconductor parametric analyzer (SPA), respectively. The SMU is used to bias and hold an injection current of an element while the SPA varies the current of the other element and measures the voltage across its cavity making a single LIV. An example of a single SPA LIV measurement is shown in Fig. 3.4. By acquiring similar LIV data for varying fixed current into the other cavity, a 2-dimensional set of data can be obtained. The microscope turret of the probe station includes

objectives with a CMOS camera on top as well as a photodetector connected to the SPA through an optical fiber for output power data acquisition. The photodetector can also be connected to the optical spectrum analyzer (OSA) for spectral measurements of the optical output.

Because tens to hundreds of thousands of current bias points (e.g. 250-by-250 for each two-dimensional sweep) are measured for each 2x1 array, LabVIEW modules, made by present and previous students in the group, are used to control the SMU and SPA to automatically perform the bias sweep and organize the voltage and light intensity output measurements into text files. These data vectors are simply reorganized into two-dimensional matrices of data arising from the two independent current injections.

The following was the procedure followed for LIV characterization. An initial individual sweep of each element is conducted to characterize one of the elements in an array. From this characterization, the rollover current, the current at which a VCSEL reaches maximum output power and intensity begins to fall off, is also determined. Biasing elements past their rollover current puts them at risk of permanent damage from thermal effects, so they are not biased beyond this point.

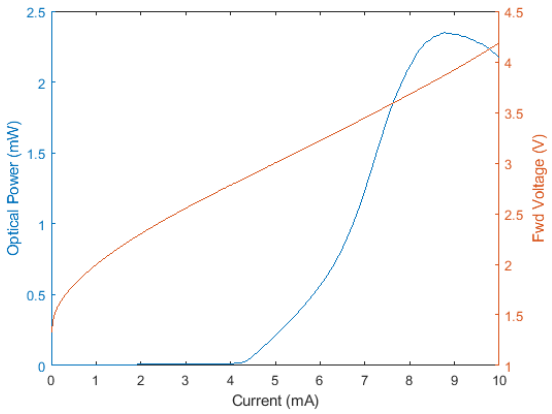

Figure 3.4 Single element LIV output of a semiconductor parametric analyzer (SPA) measurement. 2D LIV data are constructed from multiple of such measurements. Rollover occurs at ~8.6 mA.

3.3 Far-Field Measurement

For far-field spatial distribution measurements the light output is free-space coupled to a goniophotometer. To calibrate, the photometer is positioned sufficiently far from the lasing device, approximately six inches above, to ensure measurement is out of the near-field regime. The device under test is biased such that both elements are lasing but emit an approximately Gaussian distribution and are thus out of the coherent coupling regime. Following this alignment and calibration, another LabVIEW code controls the automated sweep and measurement of the far-field spatial distribution within a two-dimensional array of current biases. Figure 3.5 shows the goniometer aligned to couple to the VCSEL emission to perform far-field measurements.

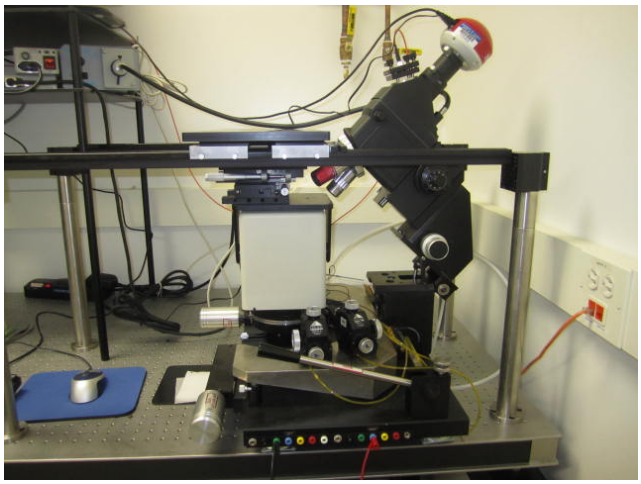

Figure 3.5 Alessi Probe Station in far-field measurement mode. The microscope head and photodetector are lifted to couple the emission into the goniometer (white box).

4. Description and Analysis of Research Results

In this chapter, the optical measurements of the coherent VCSEL arrays are reviewed, an algorithm for analyzing the raw acquired data is discussed, and the results are explained. The same process is also employed for the electrical measurements. The collected data of light intensity and voltage as a function of current is analyzed as a function of the two independent bias currents. Specifically, the current to one element of the array is independently varied while the other element is held at a fixed current. In taking this perspective, the light versus current (LI) curves can be compared to the LI behavior of a single element in the absence of current in the other device element. Figure 4.1(a) is an example of this analysis.

4.1 Optical Output Intensity Analysis

Shown in Fig. 4.1(a) is the LI characteristic for one element of the array while the bias current to the other element is held at 0 or a fixed current. Notice that at approximately 6.1 mA a small peak appears when both elements are biased. This peak arises when the two lasing elements are coherently coupled and disappears when they are not (even if both elements are above lasing threshold). This single peak has not only been correlated to coherent coupled operation, but the offset in optical intensity has also been used to calculate degree of coupling in the form of the imaginary part of the coupling coefficient [3]. The appearance of this peak is a direct consequence of coherent coupling between the elements, and we wish to identify the current range over which coherent operation is obtained.

From the L-I characteristic, an algorithm is employed to identify the region of coherent coupling over which the additional offset power is recognizable. To isolate this power “bump”, a local regression

smoothing model is used to fit the curve, where the "bump" is excluded from the fit. The "**R**obust **LO**cal **W**eighted reg**ESS**ion" (RLOWESS) smoothing method, provided in MATLAB's library of functions, with a span parameter of α=.13, was found to provide the best fit to the curve while segregating the desired bump. RLOWESS is a local regression that employs weighted linear least squares to fit data that also excludes outliers in data "outside six mean absolute deviations." The span, 0≤α≤1, is the percentage of the total number data points included in the subset that is weighted and used to determine a smoothed value. An α value that is too small fits "too well" and fails to remove outliers and random fluctuations in the measurement. A value too high will tend to smooth the data and remove the interesting behavior.

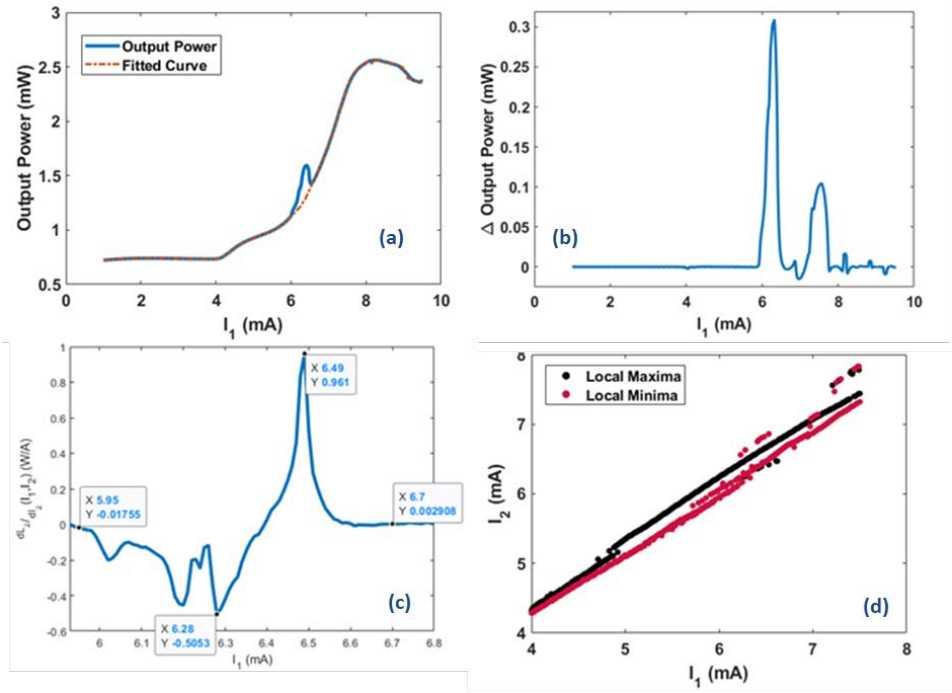

Figure 4.1 (a) Light output versus current I_1 for fixed I_2=5.36mA (blue) and RLOWESS fit (orange). (b) Plot of isolated output bump calculated by subtracting measured curve from RLOWESS fit; (c) Derivative of (b) where the minimum and maximum are marked in red and black dots respectively. (d) Plot of the minimum and maximum curvature points for varying I_1 with fixed I_2.

Figure 4.1(a) shows an example measured LI and the resulting fitted curve. The fit is subtracted from the raw data to obtain an isolated offset power peak near I=6.1mA, as shown in Fig 4.1(b) (the second peak at approximately 7.5mA is an artifact from the curve fitting). When the peak is analyzed as a Lorentzian lineshape, its derivative can be used to obtain the bias currents corresponding to the maximum and minimum curvature, as depicted in Fig. 4.1(c). The currents that correlate to the maximum (black) and minimum (red) curvature are taken as the boundaries of the locking regime of the coherent array. These points are extracted from each LI measurement and are plotted in Fig. 4.1(d). Therefore, the current biases that fall within the region defined by the black and red points in Fig. 4.1(d) correspond to coherent array operation. The coherent coupling region is generally found for $I_1 = I_2$ (where I_1 and I_2 are both above threshold). Figure 4.2 shows the single element LIV for each element in an array, demonstrating the asymmetry of the elements. For this particular array, I_2 is larger than I_1 in the coupled regions, which reflects the asymmetry of the elements; the right element I_2 typically needs more injected current to achieve the same output intensity in the right element.

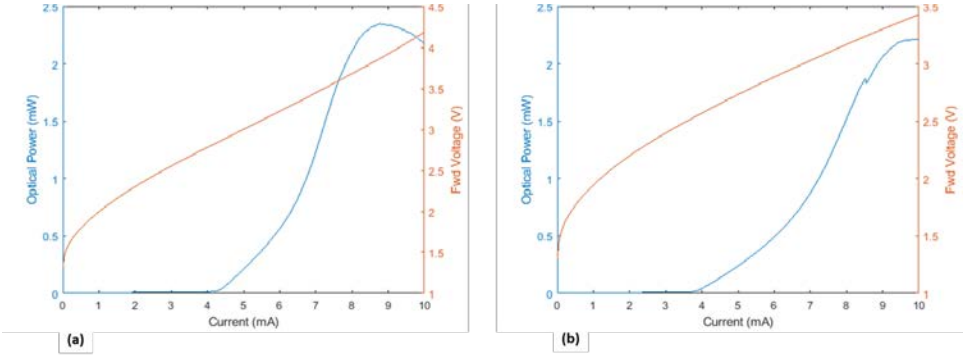

Figure 4.2 Single element LIV of the (a) left and (b) right elements of a 2 x 1 VCSEL array. For the same current bias, the left element emits higher intensity than the right.

4.2 Electrical Derivative Analysis

A similar analysis can be applied to the measured voltage data, but there are no notable features that can be correlated to coherent coupling. However, when the gradient of the voltage is taken with respect to its corresponding current, new features in the differential resistance are revealed. Figure 4.3 shows the derivative of each voltage with respect to its current plotted against both I_1 and I_2. A ridge along the diagonal is distinguishable in Fig. 4.3(a) and (b) that seems to correspond to the region of coherent coupling. The analysis that follows will confirm this hypothesis. Looking more closely at 4.3(a), in the bottom left quadrant, as I_1 increases the voltage derivative in the ridge moves from high differential resistance (yellow) to low (blue). In the upper right quadrant, corresponding to higher current biases, the opposite is the case.

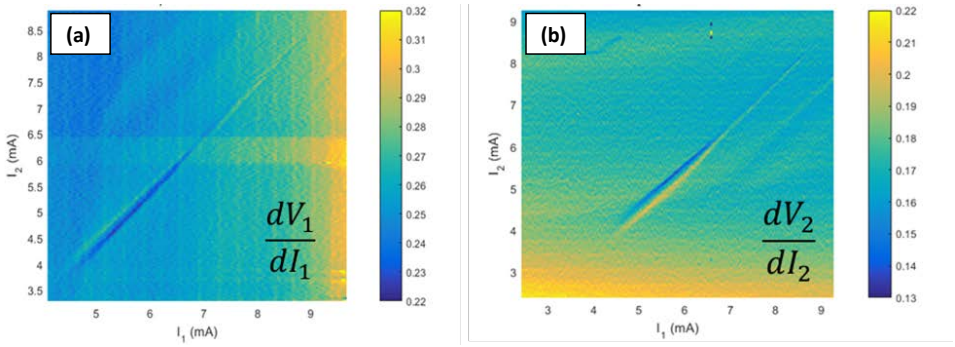

Figure 4.3 (a) I Derivative of voltage across Element 1 (dV_1) taken with respect to injection current in element 1 (dI_1). (b) Derivative of voltage across Element 2 (dV_2) taken with respect to injection current in element 2 (dI_2)

As with the output power, a similar analysis method is employed for the voltage data. Figure 4.4(a) shows the V_1 derivative taken with respect to I_1. Note the voltage data has noise that produces significant noise seen in the derivative. An RLOWESS fit is employed to fit the curve for extracting the maximum and minimum (see dotted curve in Fig. 4.4(a)). Again the fit is subtracted from the raw data. Due to the noise, a second RLOWESS fit is taken, this time to smooth the data. The currents at the maximum and minimum of the derivative points are taken as defining the coherent operation of the array as determined by the electrical data.

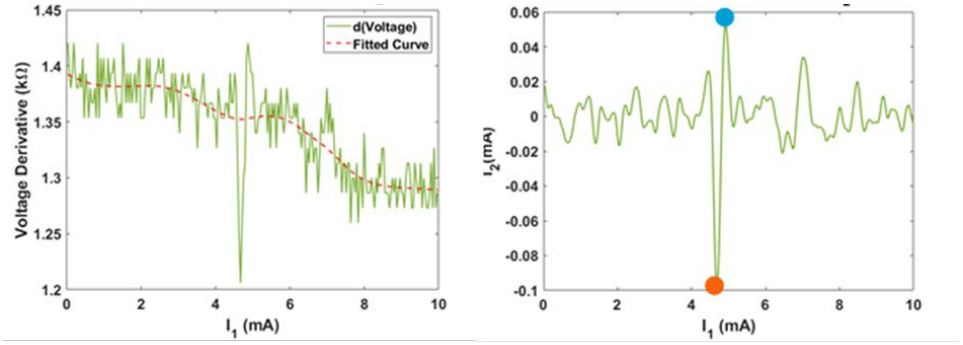

Figure 4.4 (a) Derivative of V_1 with respect to I_1 for fixed I_2 (green) with RLOWESS fit (orange). (b) dV_1 with RLOWESS fit subtracted and then smoothed using RLOWESS to smooth rather than fit. Maximum point (blue) and minimum point (orange) marked. Those very points will be taken for plotting in Figure 4.4.

The currents corresponding to the maximum and minimum of the voltage derivative are extracted for all values of I_1 and I_2 above threshold and are plotted in Fig. 4.5. In the next section, we compare the coherent operation regimes as determined by the light intensity versus the differential resistance.

An additional interesting behavior is revealed in the differential resistance data. Notice in Fig. 4.5 that the current at the maximum corresponds to lower I_1 values than the minimum for the lower values of fixed I_2. That is, in Figure 4.5(a) for $I_2 < 5$ mA, the blue points appear to the left of their

corresponding orange points. For $I_2 > 5$ mA, the maximum value points follow the same trend, but the minimum points appear at a lower I_1 injection (i.e. orange points appear to the left of blue points). Thus, for I_1 and I_2 both approximately equal to 5 mA, a change in the array modal behavior is indicated. In prior experiments, modal bistability between the in-phase and out-of-phase coupled mode were identified [18]. The data of Fig. 4.5 suggests a similar phenomenon indicative of a sudden change in coupling behavior between the two elements. At current biases greater than 7 mA, the coherent coupling region becomes less distinct, where the signal of the electrical line shape is lost in the noise and is no longer accurately detected by the algorithm.

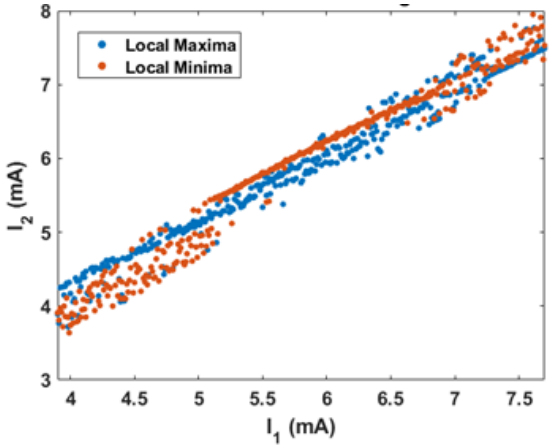

Figure 4.5 Electrical differential resistance ridge region of maxima and minima in the voltage derivative for each value of fixed I_2.

4.3 Correlation of Optical and Electrical Characteristics

The primary goal of this work is to determine whether the optical phenomenon of coherent coupling between two lasers can be detected in the electrical properties. The differential voltage ridge region seen in Fig. 4.5 is compared with the optically-determined coupling region from the offset power

obtained in Fig. 4.1(d), and both are plotted together in Fig. 4.6. As is apparent, the array coherence regimes as defined by the two approaches overlap significantly. The electrical ridge region is noticeably less defined than that in the optical intensity, which is consistent with the smaller signal-to-noise ratio in the differential resistance data. As a result, the coupled region is still well-defined from the algorithm up to current biases near 8 mA, whereas dependable knowledge of the voltage ridge boundary is lost near 7 mA biases. The two regions share some other exceptional features. In the region where 5.5mA ≤ I_1 ≤ 6.5mA, the maximum bias points in both differential voltage and light offset demonstrate some instability between two lines of I_2 vs I_1. Notably, this region of current biases corresponds to the largest peak offset power in the optical intensity.

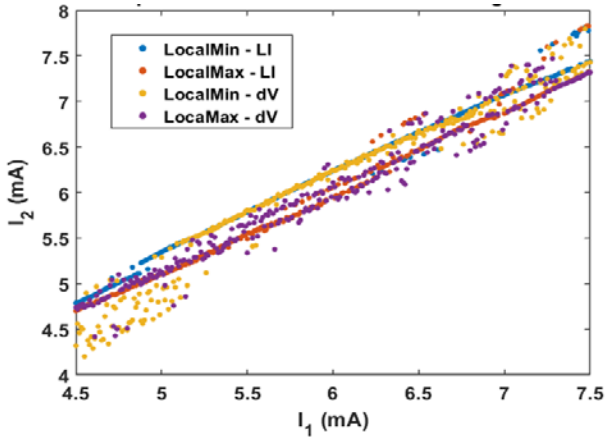

Figure 4.6 Voltage derivative boundary points (Figure 4.4) plotted together with optical offset coupling boundary points (Figure 4.1(d)).

Most importantly, however, it can be concluded that the ridge observed in the differential voltage does indeed correspond to the optically-defined coupling region and can thus be referred to as the electrically-defined or voltage derivative-defined coupling region. The scatter plot in Fig. 4.7 shows select biases corresponding to high degrees of coherence between the two elements, determined by high visibility in the far-field distribution. These measurements correspond to a device different from those shown previously. The blue circles correspond to out-of-phase points, where the field null occurs at the center of the distribution while the side-lobes exhibit high brightness. The points marked by a red 'x' denote in-phase coupling where the largest intensity occurs on center with significant side-lobes. The dominant mode switches from out-of-phase to in-phase when (I_1, I_2) = (6.0, 6.5) mA.

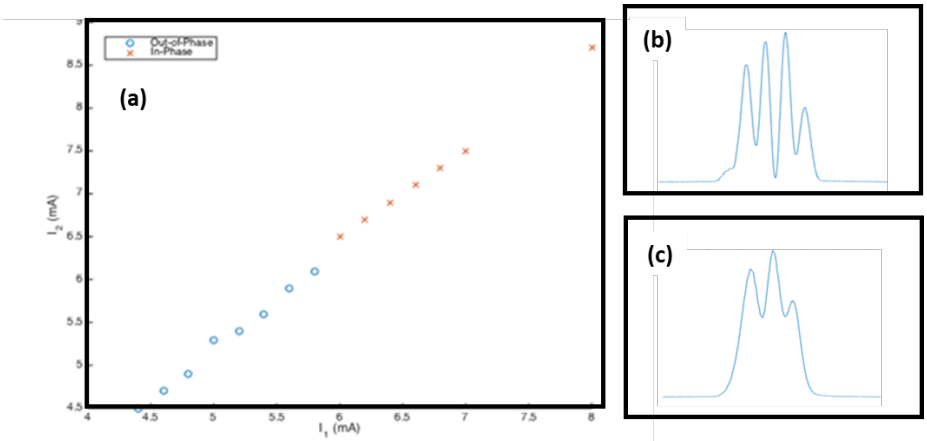

Figure 4.7 (a) Select points in the I_2-I_1 scatter plot corresponding to high visibility far-field spatial distributions. An (o) corresponds to an out-of-phase mode distribution shown in (b) with a on-axis null and an (x) corresponds to an in-phase mode distribution shown in (c) with an on-axis peak.

In Fig. 4.8 some of those points are taken and marked on a 2D surface plot of the differential series resistance. These points land well within the voltage derivative ridge. Most notably, the switch from out-of-phase to in-phase mode seen in the far-field aligns with the swapping in extrema seen in the voltage derivative ridge. Thus, the voltage derivative data appears not only to demonstrate an electrical series resistance "signature" to indicate coherent coupling, but also to reflect optical phenomena such as a change in dominant lasing mode.

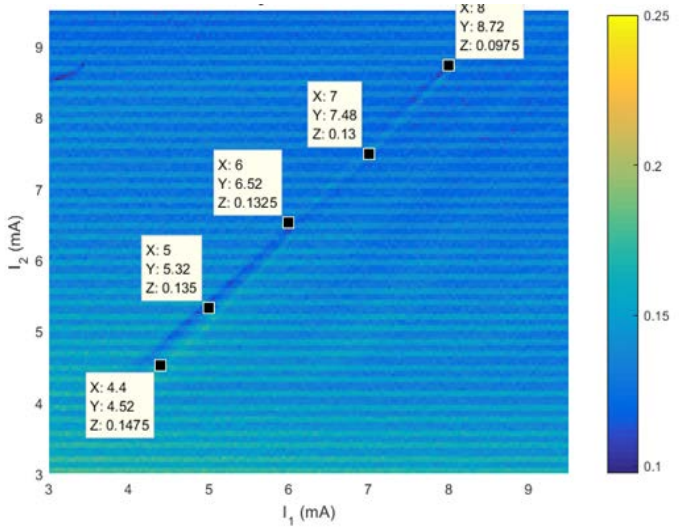

Figure 4.8 2D voltage derivative surface plot with data cursors corresponding to same points with structured far-field distributions from Figure 4.7. The horizontal stripes are a result of measurement artifacts.

5. Conclusion

This work has demonstrated that coherent operation between the elements of a 2x1 VCSEL array can be recognized in electrical measurements as a “signature” observed in the differential resistance. Additionally, this electrical signature, as well as the bump in the output light intensity, can be used to determine a region of coherent coupling as demonstrated via a simple derivative and line shape analysis. The regions determined from the output intensity as well as the voltage derivative have been shown to correspond to each other as well as to measurements shown in the far-field. Additional curve fitting techniques may be used to describe the series resistance feature and the possibly the device behavior that causes these results, possibly a Lorentzian line shape.

Having established an electrical signature for the onset of coherent operation in the VCSEL arrays, future work should consider whether this signal can be used to maintain coherent operation. VCSEL arrays in coherent coupled operation are an emergent technology that holds promise for the advancement of VCSEL in current, as well as future, applications. Hence the ability to lock these arrays into coherent operation may be important for their deployment.

References

[1] K.Iga, "Surface emitting laser-its birth and generation of new optoelectronics fields", IEEE J. Sel. Topics Quantum Electron. **6,** 1201-1215, 2000.

[2] The History of VCSEL Technology, web page. Finisar Corporation. Available at: https://www.finisar.com/products/sensing-components/vcsels. Accessed April 19, 2019.

[3] K. D. Choquette and K. M. Geib, Fabrication and performance of vertical cavity surface emitting lasers, Chapter 5 in *Vertical Cavity Surface Emitting Lasers,* ed. C. Wilmsen, H. Temkin, and L. Coldren (Cambridge University Press, Cambridge, UK) 1999.

[4] VCSELs – Technology, Industry and Market Trends 2018, web page. Yole Développement. Available at: https://www.i-micronews.com/products/vcsels-technology-industry-and-market-trends/?cn-reloaded=1 Accessed February 22, 2019.

[5] Imaging Infrared: Apple iPhone X – Infrared Dot Projector, webpage. Systems Plus Consulting. https://www.systemplus.fr/reverse-costing-reports/apple-iphone-x-infrared-dot-projector/ Accessed February 22, 2019.

[6] S. T. M. Fryslie, M. P. Tan, D. F. Siriani, M. T. Johnson, and K. D. Choquette, "37 GHz Modulation via Resonance Tuning in Single Mode Coherent Vertical Cavity Laser Arrays," IEEE Phot. Tech. Lett. **27**, pp. 415-418 (2015).

[7] S. T. M. Fryslie, Z. Gao, H. Dave, B. J. Thompson, K. Lakomy, S. Lin, P. Decker, D. McElfresh, J. E. Schutt-Aine, and K. D. Choquette, "Modulation of Coherently-Coupled Phased Photonic Crystal Vertical Cavity Laser Arrays" (invited), J. Sel. Top. Quan. Electron. **23**, 1700409 (2017).

[8] L. Mandel and E. Wolf, Coherence properties of optical fields, Rev. Mod. Phys. **37**, 231-287, 1965.

[9] D. F. Siriani and K. D. Choquette, "Implant Defined Anti-Guided Vertical Cavity Surface Emitting Laser Arrays," IEEE J. Quant. Electron. **47**, pp. 160-164 (2011).

[10] S. T. M. Fryslie, M. T. Johnson, M. P. Tan, and K. D. Choquette, "Coherence Tuning in Optically Coupled Phased Vertical Cavity Laser Arrays," IEEE J. Quan. Electron. **51**, 2600206 (2015).

[11] B. J. Thompson, Z. Gao, S. T. M. Fryslie, M. T. Johnson, D. F. Siriani, K. D. Choquette, Coherence in Multielement-phased vertical-cavity surface-emitting laser arrays using resonance tuning, IEEE Photonics Journal, **9**, 1-8, 2017.

[12] Z. Gao, B. J. Thompson, H. Dave, and K. D. Choquette. The complex coupling coefficient of coherent vcsel arrays. 2019 IEEE International Semiconductor Laser Conference, 2018, DOI: 10.1109/ISLC.2018.8516185

Formatted: Indent: Hanging: 3.26 ch, Left 0.01 ch, First line: -3.26 ch, Space After: 0 pt

[13] T. L. Paoli. Observation of second derivatives of the electrical characteristics of double-heterostructure junction lasers, Transaction on Electron Devices. **23**, 1333-1336, 1976.

[14] P. A. Barnes and T. L. Paoli, Derivative measurements of the current-voltage characteristics of double heterostructure injection lasers, IEEE J. Quant. Elec. **12**, 633-639, 1976.

[15] T. L. Paoli. Theoretical derivatives of the electrical characteristic of a junction laser operated in the vicinity of threshold, IEEE J. Quant Elec. **14**, 62-68, 1978.

[16] R. W. Dixon, Derivative measurements of light-current-voltage characteristics of (al,ga)as double-heterostructure lasers, The Bell System Technical Journal, **55**, 1-8, 1978.

[17] J. LI, J.-F. Seurin, and S. L. Chuang; K. D. Choquette, K. M. Geib, and H. Q. Hou. Correlation of electrical and optical characteristics of electively oxidized vertical-cavity surface-emitting lasers, Appl. Phys. Lett. **70**, 14, 1997.

[18] Z. Gao, S. T. M. Fryslie, B. J. Thompson, P. S. Carney, and K. D. Choquette, Parity-Time Symmetry in Coherently Coupled Vertical Cavity Laser Arrays, Optica **4**, pp. 323-329, 2017 also arXiv 1610.01657v1 (2016).